Optimal open-loop near-field control of plasmonic nanostructures

2012 New J. Phys. 14 033030

(http://iopscience.iop.org/1367-2630/14/3/033030)

New Journal of Physics
The open-access journal for physics

Optimal open-loop near-field control of plasmonic nanostructures

Martin Aeschlimann[1], Michael Bauer[2], Daniela Bayer[1], Tobias Brixner[3,6], Stefan Cunovic[4], Alexander Fischer[1], Pascal Melchior[1], Walter Pfeiffer[4], Martin Rohmer[1], Christian Schneider[1], Christian Strüber[4], Philip Tuchscherer[3] and Dmitri V Voronine[4,5]

[1] Fachbereich Physik and Research Center OPTIMAS, Technische Universität Kaiserslautern, Erwin-Schrödinger-Strasse 46, 67663 Kaiserslautern, Germany
[2] Institut für Experimentelle und Angewandte Physik, Universität Kiel, Leibnizstrasse 19, 24118 Kiel, Germany
[3] Institut für Physikalische und Theoretische Chemie, Universität Würzburg, Am Hubland, 97074 Würzburg, Germany
[4] Fakultät für Physik, Universität Bielefeld, Universitätsstrasse 25, 33615 Bielefeld, Germany
E-mail: brixner@phys-chemie.uni-wuerzburg.de

New Journal of Physics **14** (2012) 033030 (10pp)
Received 13 December 2011
Published 19 March 2012
Online at http://www.njp.org/
doi:10.1088/1367-2630/14/3/033030

Abstract. Optimal open-loop control, i.e. the application of an analytically derived control rule, is demonstrated for nanooptical excitations using polarization-shaped laser pulses. Optimal spatial near-field localization in gold nanoprisms and excitation switching is realized by applying a π shift to the relative phase of the two polarization components. The achieved near-field switching confirms theoretical predictions, proves the applicability of predefined control rules in nanooptical light–matter interaction and reveals local mode interference to be an important control mechanism.

[5] Present address: Institute for Quantum Science and Engineering, Texas A&M University, College Station, TX 77843-4242, USA.
[6] Author to whom any correspondence should be addressed.

Contents

1. Introduction

Ultrafast control of nanophotonic excitations on a subdiffraction length scale offers routes toward integrated high-speed optical interconnects. In particular, plasmonic excitations, i.e. resonant plasmon polaritons of metal nanostructures, are of interest for future applications in chip technology [1]. For these plasmonic devices the coupling between the far field, i.e. the macro-world, and the nanoscale excitations is essential, and optical resonant nanoantennas are developed to efficiently couple light to plasmonic nanostructures [2–4]. Nanoantennas are promising candidates for single-molecule applications [5], high-harmonic generation radiation sources in the extreme ultraviolet [6] and nanophotonic circuitry [2, 7, 8]. All degrees of freedom of the incident light affect the local excitations and thus offer the possibility of coherently controlling nanophotonic excitations in both space and time [9]. In addition to the spectral/temporal phase of the incident light field [10, 11], the polarization degree of freedom was shown to be essential for simultaneously achieving spatial and temporal control [9, 12–14]. With the increasing complexity of the nanostructure it becomes, however, less obvious how a particular spatiotemporal excitation can be achieved using suitably shaped incident light. Although two-pulse correlation measurements [15], parameter scans [11, 14], time-reversal concepts [16, 17] and adaptive optimization methods [12, 13] provided successful demonstrations of nanoplasmonic control, it is essential to develop a basic understanding of the control mechanisms and devise predefined rules to control local excitations. A particularly important issue is the question of how optimal control can be achieved, i.e. how the global optimum can be found. Until now only closed-loop control schemes have provided this capability in experiments. It is exactly these aspects that are addressed here. The here-demonstrated optimal open-loop control, i.e. the application of an analytically derived control rule, facilitates the future design of optimized plasmonic nanostructures that will allow realization of particular spatiotemporal nanophotonic excitations, such as, for example, ultrafast high-contrast switching below the diffraction limit.

2. Results and discussion

In a recent theoretical investigation of propagating modes in a branched T-shaped nanoparticle waveguide structure, we developed an analytic approach for nanoplasmonic control and demonstrated open-loop control of spatial excitation switching [18]. Optimal switching between the local linear flux in a nanostructure is achieved if the difference in the spectral phases of the two incident laser pulse polarization components is changed by π. Irrespective of the nanostructure shape, the interference of different excited modes is the underlying control mechanism. Here we demonstrate this theoretical concept of an analytically derived predefined

control rule in an experiment by optimal switching of the excitation between two corners of a triangular gold nanoprism. This nanostructure is highly attractive for control experiments because it has a complex response with several modes [19–21]. In a recent experiment we adjusted the relative time delay between two different polarizations and observed the constructive and destructive interference of such modes [22]. However, as opposed to the single-parameter control there, in the experiment presented here a more general multidimensional parameter space provided by polarization-shaped laser pulses is considered. This enables us to account for the complex response function of the gold nanostructure such that the relative phase between the two polarizations can be modulated separately for each frequency.

We investigate a triangular gold nanoprism with 400 nm side length and 40 nm height. The nanoprisms were prepared by e-beam lithography on an ITO/glass substrate. By dosing the nanoprisms with Cs, the work function of the gold surface was reduced below 4.6 eV to enable two-color two-photon photoemission for the given pump and probe photon energies. Two-photon photoemission electron microscopy (2P-PEEM) [23] was used to monitor the local near field with spatial resolution < 40 nm, i.e. on a subwavelength scale, by measuring spatial distribution patterns of electrons emitted from metal surfaces under photoexcitation.

The experimental setup is similar to a previously reported one [9] but modified to allow for two-color two-photon excitation that avoids interference effects between the pump and the probe, and ensures that the one-photon pump excitation at 1.6 eV is probed homogeneously across the nanostructure. Light pulses are generated by a Ti:sapphire oscillator (80 MHz, 795 nm and $\sim$30 fs full-width at half-maximum (FWHM)). One part is frequency doubled in a 300 μm beta-barium borate (BBO) crystal, and a transform-limited s-polarized 30 fs (FWHM) laser pulse with 398 nm central wavelength (corresponding to a photon energy of 3.1 eV) is directed onto the sample (probe). The other part (pump) is polarization shaped [24] and overlapping under a small angle ($\sim 1^\circ$) with the probe beam on the sample at 65° angle of incidence. The polarization-shaped pulses (central wavelength 795 nm) are characterized using dual-channel spectral interferometry with reference pulses measured via FROG and SPIDER [25].

The PEEM pattern generated by probe pulse-induced two-photon photoemission (2×3.1 eV) alone reveals a homogeneous emission from the nanoprism surface (not shown), proving that the whole nanostructure area is uniformly probed. However, upon excitation with a polarization-shaped pump laser pulse in temporal overlap with the probe pulse, the photoemission signals localize at particular spatial regions on the nanoprism. In addition, the emission is about threefold enhanced compared to the background of two-photon photoemission due to uncorrelated pump and probe pulses. Under these conditions, the 2P-PEEM pattern reveals the joined excitation probability of the pump and the probe. Either the polarization-shaped pump pulse generates, via linear absorption, a distribution of excited electrons that is then homogeneously probed, or the probe pulse generates a homogeneous excitation, which is then locally promoted into the electron continuum. In both cases the observed emission pattern reveals the local one-photon pump interaction. Thus, although a nonlinear method is used, we investigate the linear response of the nanoprism at the pump wavelength.

For the adaptive optimization we use an evolutionary algorithm [26]. The feedback for the optimization is derived from the measured two-color 2P-PEEM patterns. Adaptive optimizations are performed using spectral phase shaping of each polarization component, i.e. no spectral components are attenuated. The spectral phases $\phi_i(\omega)$ are parameterized independently using a sixth-order Taylor expansion with the absolute phase of one polarization component set constant. Thus 11 independent parameter genes are varied and optimized in the

adaptive learning loop. We used 40 individuals per generation, and convergence was usually reached after 20–40 generations. During the optimization process small lateral drifts of the sample occurred and were compensated for by a drift correction previous to the evaluation of each generation using reference photoemission patterns recorded with unshaped pulses.

To demonstrate optimal open-loop nanoplasmonic excitation control in an experiment, we first adaptively optimize the photoemission pattern of a triangular gold nanoprism and then apply the predefined analytic control rule derived from our theoretical considerations (figure 1) [18]. As an optimization goal the emission ratio from two corners (regions of interest (ROI) ROI 1 and ROI 2 in figures 1(c) and (e)) of the nanoprism was maximized. The corresponding fitness function is defined as the ratio $f_{\mathrm{Mean}}^{\mathrm{Max}} = \mathrm{Max(ROI\,1)/Mean(ROI\,2)}$, which is calculated based on the time-integrated photoemission yield of the ROIs at the corners of the right nanoprism shown in figure 1(c). The function 'Max' chooses the pixel with highest photoemission yield in the ROI and calculates the mean yield in a surrounding region of 7×7 pixels including the maximum pixel in the center. 'Mean' takes the average value of all pixels in the ROI. Compared to other fitness functions, $f_{\mathrm{Mean}}^{\mathrm{Max}}$ enabled fast convergence while preferring high total photoemission yield. The fitness evolution during the optimization is shown in figure 1(g) (red circles). Additionally, the optimization of the opposite fitness function Max(ROI 2)/Mean(ROI 1) (blue diamonds) and the reference fitness (black crosses), i.e. the fitness achieved for an unshaped laser pulse, are indicated. The optimization started with random initial spectral phases. It is seen in figure 1(g) that the fitness in both optimizations increases continuously until the saturation is reached at generations 33 and 28, respectively. The fitness values are always greater than 1, which results from the chosen fitness functions. The different definitions of the ROIs in figures 1(c) and (e) do not significantly influence the optimization process because the 'Max' function selects the maximum-yield position.

Note that a 180° rotated nanoprism (left nanoprism in figure 1(c)) behaves differently, i.e. no emissions at the corresponding corners are observed. Hence the response of the nanoprisms is strongly dependent on the k-vector of the incident pulse, emphasizing the importance of symmetry breaking and of a combination of k-control and pulse shaping that determines the excitation pattern seen in figure 1(c). To demonstrate optimal open-loop switching, we discuss in the following the right nanoprism and show the left nanoprism only for reference.

As shown in figure 1(c), the emission is strong from ROI 1, whereas there is almost no emission from ROI 2 applying the optimal pulse from figure 1(a). Next, following our theoretically derived rule for an optimal switching contrast [18], a constant spectral phase π is added to one of the two polarization components for the entire frequency range. This corresponds to a π shift of the relative phase between both polarization components. After this open-loop control step, the pump-pulse shape (figure 1(b)) and the emission pattern (figure 1(d)) change, and indeed the strongest emission is now located in ROI 2. To verify that the thereby determined pulse shape corresponds to the global optimum for the reversed fitness function, we also applied the reverse procedure.

The results are shown in figures 1(e) and (f). Here the fitness function Max(ROI 2)/Mean(ROI 1) was adaptively maximized (pulse shape not shown) and the resulting emission pattern of the adaptively found global optimum (figure 1(e)) closely resembles the pattern obtained by the optimal open-loop control (figure 1(d)). Application of the analytic control rule switches the emission pattern back toward strong emission from ROI 1 and negligible emission from ROI 2 (figure 1(f)). Optimal open-loop controlled switching and adaptive optimization of the inverse ratio yield almost identical excitation patterns and provide

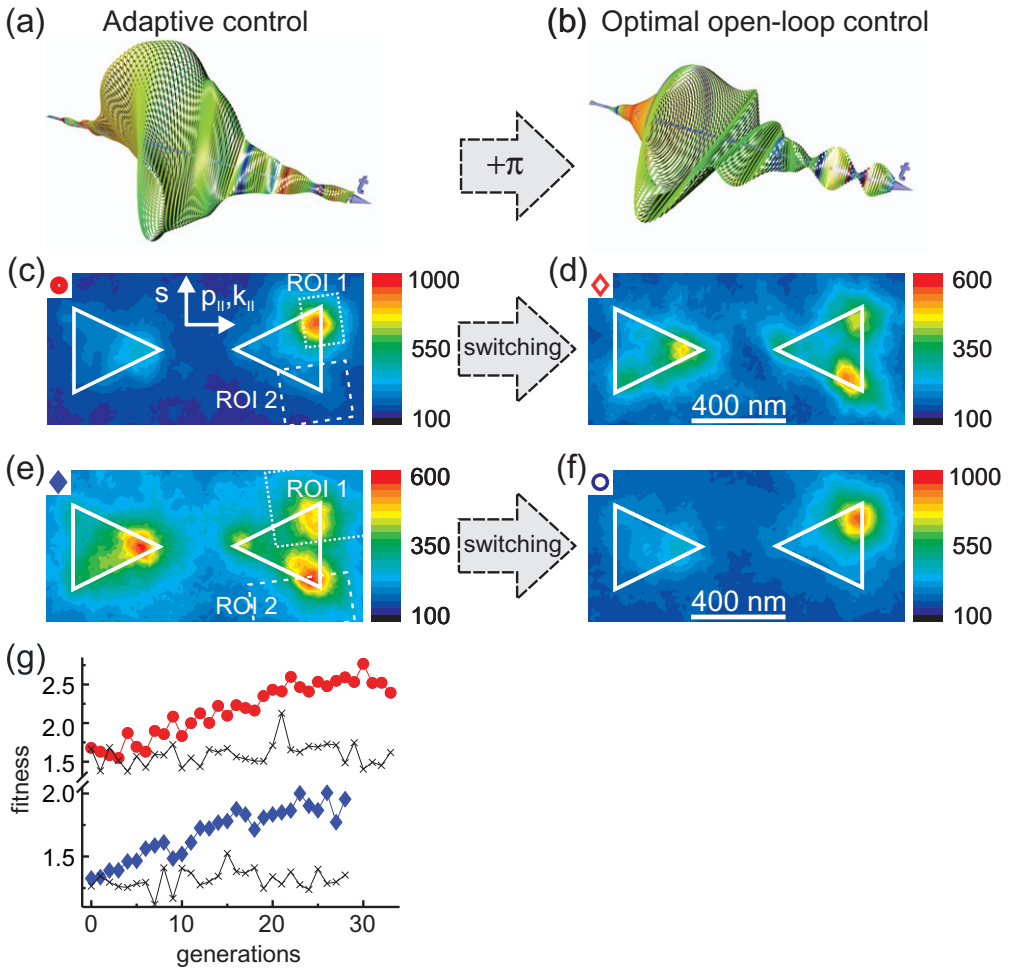

Figure 1. Adaptive (left column) versus optimal open-loop control (right column) of gold nanoprism excitations. In the adaptive approach, the optimal polarization-shaped laser pulse (a) localizes photoemission at a selected nanoprism corner, in this case ROI 1 (c). For optimal open-loop control, a spectral phase shift of π is added to one polarization component, leading to a different pulse shape (b). This results in a subwavelength spatial switching of local fields toward ROI 2 (d). Similarly, adaptive optimization can be performed (the resulting pulse shape is not shown) for localization in the lower corner ROI 2 (e), and optimal open-loop controlled switching leads back to the emission from ROI 1 (f). The projections of the laser wave vector ($k_{\|}$) and polarization components (s and $p_{\|}$) onto the plane of the sample are shown in (c). A transform-limited 3.1 eV s-polarized pulse was used as a probe in all cases ($\sim$30 fs FWHM). The actual fitness (described in the main text) of the best individual is plotted as a function of generation number for the two adaptive optimizations together with the respective reference patterns (black crosses) patterns recorded with unshaped pulses (g). The symbols in the upper left corners of (c)–(f) correspond to figure 2 and to the fitness evolution in (g).

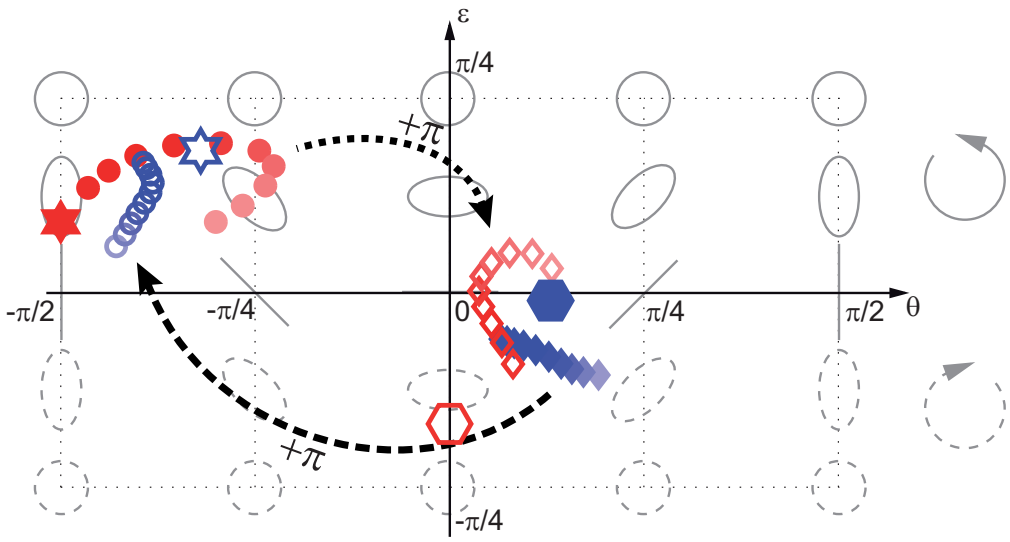

Figure 2. Optimal pulses derived either by optimal open-loop (open symbols) or adaptive closed-loop (filled symbols) control are represented in the Poincaré plane, which contains all possible polarization states of light as defined by the two parameters, orientation θ and ellipticity ε [27]. The symbols are defined in figures 1(c)–(f). The plots cover a time range from −30 to 30 fs, corresponding to the complete temporal overlap with the probe pulse. The symbol shading reflects the normalized electric field strength. The stars and hexagons represent the optimized pulses from a repeated run of the experiment. For clarity the polarization parameters are only shown for maximum overlap with the probe pulse, i.e. for pump–probe delay $\tau = 0$ fs, and should be compared to circles and diamonds, respectively.

a clear experimental demonstration of the theoretically predicted control rule. The results were verified by repeating adaptive optimizations and optimal open-loop control, which showed good reproducibility.

We now further compare and analyze the laser pulse shapes to obtain an insight into the control mechanism. For better comparison we plot the polarization-state evolution on a Poincaré surface (figure 2) [27]. This two-dimensional 'phase space' contains all possible polarization states of light as defined by the two parameters, the orientation θ and ellipticity ε, of light. The convention is such that positive and negative values of ε define left (solid lines) and right (dashed lines) elliptical polarizations, respectively, and the angle θ is the orientation of the ellipse. Various momentary polarization states of light are shown as circles and ellipses in different parts of the plot in figure 2. The temporal evolution of the polarization state as the pump pulse evolves from −30 to 30 fs is segmented in ten time bins, and the momentary polarization states of these bins are represented by points on the Poincaré surface. These data points, i.e. the time window from −30 to 30 fs, cover the temporal overlap between the pump and probe pulses. Adaptively optimized (solid symbols) and optimal open-loop pulses (open symbols) for the same control objective overlap in the same regions of the Poincaré plot, indicating that the open-loop control reaches indeed the global optimum for excitation switching. The good repeatability of optimal open-loop control is also indicated in figure 2, showing in addition the

optimal pulse shapes of a repeated run of the experiment. For clarity the optimized pulses are shown as single symbols representing the polarization parameters $\{\theta, \varepsilon\}$ of the polarization-shaped pump pulse for maximum overlap with the probe pulse, i.e. for vanishing delay τ between pump and probe pulses ($\tau = 0$ fs). The adaptively (analytically) optimized pulse for localization at ROI 1 is indicated as a full red (open blue) star. The corresponding polarization parameters for localization at ROI 2 are given as full blue and open red hexagons, respectively. Within the experimental uncertainty the corresponding pulse parameters are localized in the same regions of Poincaré space, demonstrating good repeatability of the applied optimization schemes.

Under ideal circumstances, the π phase shift should result in an inversion of the pulse with respect to the center (0, 0) of the Poincaré surface. As can be seen in figure 2, the inversion is not perfect due to pulse modification effects upon propagation through the pulse shaper and other optical elements on the way toward the sample. Such effects can be understood using a frequency-dependent Jones matrix, which is appropriate for linear optical elements and has been described in detail elsewhere [24]. The data in figure 2 have been obtained directly from dual-channel spectral interferometry. It is notable that the optimal pulse for signal localization in ROI 1 tends to be circularly polarized, while that for ROI 2 is more linearly polarized. This asymmetry is attributed to an asymmetry of the real nanostructure, i.e. deviations from the ideal triangular shape for which a symmetric behavior is expected. However, the evolutionary algorithm still finds optimal pulses that provide a good degree of control in both directions, and the optimal open-loop control rule approach also works.

To compare the results of the adaptive closed-loop and open-loop control rule-based optimizations and to obtain insight into the control mechanism we discuss the response of the nanoprism in more detail. The nanooptical excitations are localized in subwavelength regions at the nanoprism corners and allow switching via polarization control. This control is possible via either matching the orientation of the incident polarization to a local dipole or via the interference of the local fields generated by the two independent polarization components [28].

As discussed in the following, here the latter mechanism applies and a localized mode excited by the s-polarized component interferes locally with a propagating mode generated by the p-polarized component. This control mechanism emphasizes the analogy (figure 3(a)) between nanoprisms (yellow triangle) and branched waveguide structures (gray spheres). In the case of normal incidence the orientation of the electric field vector with respect to the edges of the triangle determines the resulting near-field distribution. If the electric field is oriented along a nanoprism edge, a dipole mode parallel to this edge is excited, leading to strong field enhancements at the corners of this edge [29], i.e. in ROI 1 and ROI 2. For an electric field perpendicular to one edge, a relatively weak near-field enhancement along this edge and a strong enhancement at the opposite corner are observed [30]. In the present case the non-normal incidence breaks symmetry and the emission pattern for p-polarized illumination differs from this behavior (figures 3(b) and (c)). The two-color 2P-PEEM images reveal the near-field distribution of the triangular nanoprism under illumination by an unshaped transform-limited p-polarized pump pulse (1.6 eV photon energy) and change with the wave vector orientation with respect to the nanoprism (figures 3(b) and (c)). The highest field strength always appears at the corners of the triangle opposite to the incoming wave. This suggests that propagation or retardation effects significantly influence the actual field distribution. We therefore suggest that the incident wave interacts with the edges of the nanostructure and launches propagating modes that then focus in the opposing corners of the triangle, leading to strong field enhancements

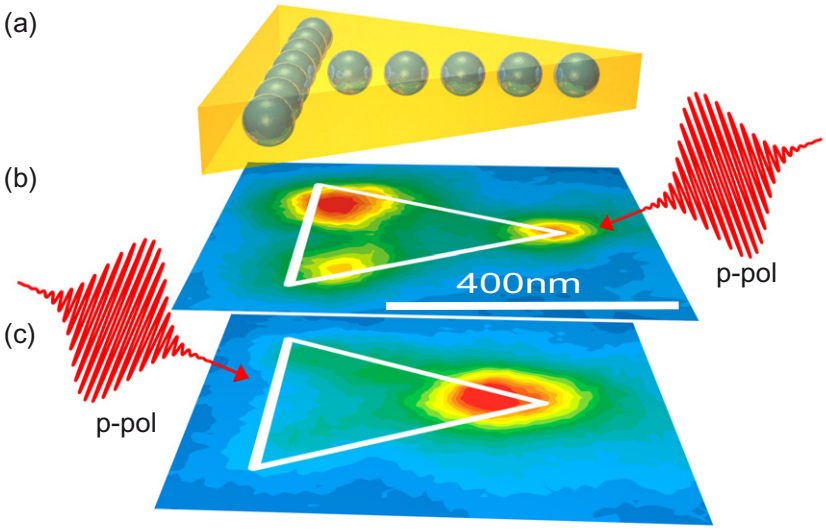

Figure 3. (a) Gold nanoprism with 400 nm side length and 40 nm height. The nanoprism is overlapped with an example of a plasmonic nanoparticle chain waveguide to highlight similarities of the near-field control behavior. (b), (c) Two-color two-photon photoemission electron microscope images of the gold nanoprism from (a) under illumination by a transform-limited p-polarized 1.6 eV pump laser pulse (∼30 fs FWHM) at 65° angle of incidence for an incident wave vector (arrow) from right (b) and left (c). A transform-limited 3.1 eV s-polarized pulse was used as a probe (∼30 fs FWHM).

in the corners, i.e. in ROI 1 and ROI 2 (figure 3(b)). The excitation patterns generated by s- and p-polarized excitations overlap and we therefore conclude that the achieved control of the switching in nanoprisms is mainly caused by coherent propagating modes and their interference with a localized mode excited with s-polarized light. This is supported by the similarities in the near-field control behavior of nanoprisms and waveguides and will be substantiated in a forthcoming publication. Nanooptical switching was demonstrated in theoretical investigations for branched plasmonic nanoparticle waveguides as they are depicted schematically in figure 3(a) [14, 18]. In a waveguide structure, the direction of the propagating modes and thus also the resulting near-field distribution is determined by the direction of the incident fields. This suggests that under p-polarized illumination also for the nanoprisms a broadband coherent superposition of propagating modes which critically depend on the *k*-vector orientation of the incident light are responsible for the efficient high-contrast switching of the optical near-field distribution at the corners of the nanoprism.

3. Conclusion

In summary, we provide the first experimental demonstration of optimal open-loop control of nanooptical excitations. Although applied here to achieve near-field localization and switching in a gold nanoprism, the method is general and is not restricted to that particular geometry. If the optical response of a plasmonic nanostructure is not known, the optimal open-loop approach may be used together with an adaptive optimization to achieve near-field control and switching.

If the complete spectral response is known, the first adaptive optimization step is not necessary. In addition, the nanoscale switching achieved demonstrates experimentally the proposed optical near-field control via the local interference of optical propagating and localized near fields driven by the two independent incident polarization components. Near-field coherent control by analytic pulse shaping is expected to improve the controllability of ultrafast nanooptical light–matter interactions and will help us to design novel nanophotonic devices, realize active control of plasmonic nanocircuits, and develop single-molecule, nanophotonic biosensors and other spectroscopic applications. A high degree of near-field control in plasmonic nanostructures such as antennas, waveguides and metamaterials might be achieved. The optimal open-loop scheme may also be useful for other scenarios, such as coherent control of molecules, when suitable response functions are available either through calculation or from (nonlinear) spectroscopic experiments.

Acknowledgments

We thank the Nano Structuring Center at the University of Kaiserslautern for support in the preparation of the nanostructures. This work was supported by the German Science Foundation (DFG) within the SPP 1391 (MA, MB, TB and WP), and EC FP7 under grant no. NMP3-SL-2008–214469_UltraMagnetron. This work was funded by the DFG and the University of Würzburg through the funding program Open Access Publishing.

References

[1] Zia R, Schuller J A, Chandran A and Brongersma M L 2006 Plasmonics: the next chip-scale technology *Mater. Today* **9** 20–7

[2] Mühlschlegel P, Eisler H-J, Martin O J F, Hecht B and Pohl D W 2005 Resonant optical antennas *Science* **308** 1607–9

[3] Taminiau T H, Stefani F D, Segerink F B and van Hulst N F 2008 Optical antennas direct single-molecule emission *Nature Photonics* **2** 234–7

[4] Novotny L and Hecht B 2006 *Principles of Nano-Optics* (Cambridge: Cambridge University Press)

[5] Kinkhabwala A, Yu Z, Fan S, Avlasevich Y, Müllen K and Moerner W E 2009 Large single-molecule fluorescence enhancements produced by a bowtie nanoantenna *Nature Photonics* **3** 654–7

[6] Kim S, Jin J, Kim Y-J, Park I-Y, Kim Y and Kim S-W 2008 High-harmonic generation by resonant plasmon field enhancement *Nature* **453** 757–60

[7] Bharadwaj P, Deutsch B and Novotny L 2009 Optical antennas *Adv. Opt. Photonics* **1** 438–83

[8] Huang J-S, Feichtner T, Biagioni P and Hecht B 2009 Impedance matching and emission properties of nanoantennas in an optical nanocircuit *Nano Lett.* **9** 1897–902

[9] Aeschlimann M *et al* 2010 Spatiotemporal control of nanooptical excitations *Proc. Natl Acad. Sci. USA* **107** 5329–33

[10] Stockman M I, Faleev S V and Bergman D J 2002 Coherent control of femtosecond energy localization in nanosystems *Phys. Rev. Lett.* **88** 067402

[11] Lee T-W and Gray S K 2005 Controlled spatiotemporal excitation of metal nanoparticles with picosecond optical pulses *Phys. Rev.* B **71** 035423

[12] Aeschlimann M, Bauer M, Bayer D, Brixner T, García de Abajo F J, Pfeiffer W, Rohmer M, Spindler C and Steeb F 2007 Adaptive subwavelength control of nano-optical fields *Nature* **446** 301–4

[13] Brixner T, García de Abajo F J, Schneider J and Pfeiffer W 2005 Nanoscopic ultrafast space-time-resolved spectroscopy *Phys. Rev. Lett.* **95** 093901–4

[14] Sukharev M and Seideman T 2006 Phase and polarization control as a route to plasmonic nanodevices *Nano Lett.* **6** 715–9
[15] Kubo A, Onda K, Petek H, Sun Z, Jung Y S and Kim H K 2005 Femtosecond imaging of surface plasmon dynamics in a nanostructured silver film *Nano Lett.* **5** 1123–7
[16] Durach M, Rusina A, Stockman M I and Nelson K 2007 Toward full spatiotemporal control on the nanoscale *Nano Lett.* **7** 3145–9
[17] Li X and Stockman M I 2008 Highly efficient spatiotemporal coherent control in nanoplasmonics on a nanometer-femtosecond scale by time reversal *Phys. Rev.* B **77** 195109
[18] Tuchscherer P, Rewitz C, Voronine D V, García de Abajo F J, Pfeiffer W and Brixner T 2009 Analytic coherent control of plasmon propagation in nanostructures *Opt. Express* **17** 14235–59
[19] Nelayah J, Kociak M, Stéphan O, Geuquet N, Henrard L, García de Abajo F J, Pastoriza-Santos I, Liz-Marzán L M and Colliex C 2010 Two-dimensional quasistatic stationary short range surface plasmons in flat nanoprisms *Nano Lett.* **10** 902–7
[20] Rang M, Jones A C, Zhou F, Li Z-Y, Wiley B J, Xia Y and Raschke M B 2008 Optical near-field mapping of plasmonic nanoprisms *Nano Lett.* **8** 3357–63
[21] Shuford K L, Ratner M A and Schatz G C 2005 Multipolar excitation in triangular nanoprisms *J. Chem. Phys.* **123** 114713
[22] Melchior P, Bayer D, Schneider C, Fischer A, Rohmer M, Pfeiffer W and Aeschlimann M 2011 Optical near-field interference in the excitation of a bowtie nanoantenna *Phys. Rev.* B **83** 235407
[23] Schmidt O, Bauer M, Wiemann C, Porath R, Scharte M, Andreyev O, Schönhense G and Aeschlimann M 2002 Time-resolved two photon photoemission electron microscopy *Appl. Phys.* B **74** 223–7
[24] Brixner T, Krampert G, Niklaus P and Gerber G 2002 Generation and characterization of polarization-shaped femtosecond laser pulses *Appl. Phys.* B **74** 133–44
[25] Trebino R 2002 *Frequency-Resolved Optical Gating: The Measurement of Ultrashort Laser Pulses* (Amsterdam: Springer)
[26] Goldberg D E 1989 *Genetic Algorithms in Search, Optimization, and Machine Learning* (Reading, MA: Addison-Wesley Professional)
[27] Brixner T 2003 Poincaré representation of polarization-shaped femtosecond laser pulses *Appl. Phys.* B **76** 531–40
[28] Brixner T, García de Abajo F J, Schneider J, Spindler C and Pfeiffer W 2006 Ultrafast adaptive optical near-field control *Phys. Rev.* B **73** 125437
[29] Kelly K L, Coronado E, Zhao L L and Schatz G C 2002 The optical properties of metal nanoparticles: the influence of size, shape, and dielectric environment *J. Phys. Chem.* B **107** 668–77
[30] Schnell M, Garcia-Etxarri A, Huber A J, Crozier K B, Borisov A, Aizpurua J and Hillenbrand R 2010 Amplitude- and phase-resolved near-field mapping of infrared antenna modes by transmission-mode scattering-type near-field microscopy *J. Phys. Chem.* C **114** 7341–5